

Iterated Perturbation Theory for Mott Insulators in a Static Electric Field with Optical Phonons

Tommaso Maria Mazzocchi* Enrico Arrigoni*

T. M. Mazzocchi, E. Arrigoni

Institute of Theoretical and Computational Physics, Graz University of Technology, Petersgasse 16/II, 8010 Graz (Austria)

mazzocchi@tugraz.at, arrigoni@tugraz.at

Keywords: *Green's functions, Strong correlation, Phonons, Quantum transport*

This Manuscript aims to compare the so-called iterated perturbation theory (IPT) and auxiliary master equation approach (AMEA) impurity solvers for a Mott insulating system driven out of equilibrium by a static electric field. Electronic heat bath and optical phonons are employed as dissipation mechanism of the current-induced Joule heat that the excited electrons of the lattice experience as the result of the field's driving. Despite its simplicity, the IPT approach yields results which are in good agreement with those obtained within the AMEA impurity solver.

1 Introduction

The last decade has witnessed an increasing interest in the physics of Mott insulating systems as they can undergo phase transitions when driven out of equilibrium by both statically and periodically electric fields.^{1–6} Due to this property, they could be used to model the so-called *insulator-to-metal transition*, which has been investigated theoretically in the seminal works^{7,8} and then observed experimentally.^{9,10} Due to their strongly interacting nature, Mott insulating systems require a nonperturbative method to be dealt with. Nowadays, the most well-established approach is given by the dynamical mean-field theory (DMFT)^{11–16} which hold under both equilibrium and nonequilibrium conditions. The DMFT relies on impurity solvers to address the nonequilibrium steady-state (NESS) of the system, which often are the bottleneck of the approach as they could be computationally costly. Purpose of this Manuscript is to benchmark the results of the iterated perturbation theory (IPT) impurity solver, which is known to work well in both the very weak and very strong interacting *regime*,¹⁷ against those obtained within the so-called auxiliary master equation approach (AMEA) impurity solver.^{18–22} The IPT solver yields results which are in quite good agreement with those obtained by employing AMEA for the very same setup in previous work.²³ The rest of the Manuscript is organized as follows: In Section 2 we introduced the model at hand while Section 3 will be devoted to a short recap of the Green's functions formalism and the IPT impurity solver. Results are discussed in Section 4 while Section 5 is left for conclusions and further considerations. The details of the physical setup under investigation and the derivation of all the relevant observables of interest can be found in the previous work from the authors.²³

2 Model Hamiltonian

We study the single-band Hubbard model in the presence of a constant electric field in the temporal gauge,²³ the Hamiltonian of which is given by

$$\hat{H}(t) = \hat{H}_U(t) + \hat{H}_{\text{bath}} + \hat{H}_{\text{e-ph}} + \hat{H}_{\text{ph}}. \quad (1)$$

We set the lattice spacing a , Planck constant \hbar and the electron charge q to one, i.e. $a = \hbar = -q = 1$. In these units the Hubbard Hamiltonian $\hat{H}_U(t)$ is given by

$$\hat{H}_U(t) = \varepsilon_c \sum_{i\sigma} \hat{n}_{i\sigma}^f - \sum_{\sigma} \sum_{(i,j)} \underbrace{t_c e^{-i(\mathbf{r}_j - \mathbf{r}_i) \cdot \mathbf{A}(t)}}_{t_{ij}(t)} \hat{f}_{i\sigma}^\dagger \hat{f}_{j\sigma} + U \sum_i \hat{n}_{i\uparrow}^f \hat{n}_{i\downarrow}^f, \quad (2)$$

where $f_{i\sigma}^\dagger$ ($\hat{f}_{i\sigma}$) is the creation (annihilation) operator of an electron of spin $\sigma = \{\uparrow, \downarrow\}$ at the i -th lattice site and $\hat{n}_{i\sigma}^f \equiv \hat{f}_{i\sigma}^\dagger \hat{f}_{i\sigma}$ the corresponding density operator. Sums over nearest neighbor sites are denoted by (i, j) . The electrons' *onsite energy* is chosen as $\varepsilon_c \equiv -U/2$ for the system to be particle-hole symmetric and t_c is the *bare* hopping amplitude. The homogeneous vector potential $\mathbf{A}(t) = -\mathbf{F} t$ is chosen such that the static electric field is constant and oriented along the body diagonal of a *hypercubic* lattice $\mathbf{e}_0 = (1, 1, \dots, 1)$ and is given by $\mathbf{F} = -\partial_t \mathbf{A}(t)$.

We take the infinite-dimension limit,^{6,24} i.e. $d \rightarrow \infty$, with the usual rescaling of the hopping $t_c = t^*/(2\sqrt{d})$, which allows to perform summations over the electron crystal momentum using the joint density of states^{25,26} $\rho(\epsilon, \bar{\epsilon}) = 1/(\pi t^{*2}) \exp[-(\epsilon^2 + \bar{\epsilon}^2)/t^{*2}]$ with $\epsilon = -2t_c \sum_{i=1}^d \cos k_i$ and $\bar{\epsilon} = -2t_c \sum_{i=1}^d \sin k_i$. An optical phonon branch is *attached* to each lattice site by means of the Hamiltonian

$$\hat{H}_{\text{e-ph}} = g \sum_{i\sigma} \hat{n}_{i\sigma}^f \hat{x}_i \quad (3)$$

with $\hat{x}_i \equiv (\hat{b}_i^\dagger + \hat{b}_i)/\sqrt{2}$, where \hat{b}_i^\dagger (\hat{b}_i) creates (annihilates) an optical phonon with energy ω_E at the lattice site i . The optical phonon Hamiltonian consists of an Einstein phonon $\hat{H}_{\text{ph,E}} = \omega_E \sum_i \hat{n}_i^b$ with $\hat{n}_i^b = \hat{b}_i^\dagger \hat{b}_i$ the phonon density, coupled to an ohmic bath $\hat{H}_{\text{ph,ohm}}$ with spectral density given in Eq. (13).

To stabilize the DMFT loop we include electronic heat baths coupled *locally* to each lattice site which are described by the Hamiltonian \hat{H}_{bath} , the details of which will be specified in Section 3.1.1, see Equation (9).

3 Methods

3.1 Green's function formalism

The Green's function (GF) approach is a versatile tool for the solution of many-body problem in- and out-of-equilibrium²⁷⁻³¹ and, as such, has been successfully applied to several systems in condensed matter over the last decade.^{1-5,32-34}

3.1.1 Electron Dyson equation

The interacting electron GF obeys the Dyson equation

$$\underline{\mathbf{G}}^{-1}(\omega, \epsilon, \bar{\epsilon}) = \underline{\mathbf{G}}_0^{-1}(\omega, \epsilon, \bar{\epsilon}) - \underline{\Sigma}_{\text{bath}}(\omega) - \underline{\Sigma}(\omega) - \underline{\Sigma}_{\text{e-ph}}(\omega), \quad (4)$$

where $\underline{\mathbf{G}}_0$ is the noninteracting GF corresponding to the Hamiltonian in Equation (2). $\underline{\Sigma}_{\text{bath}}$ is the electronic heat bath self-energy (SE), while by $\underline{\Sigma}$ and $\underline{\Sigma}_{\text{e-ph}}$ we denote the electron and electron-phonon self-energies respectively. By means of the DMFT and Migdal^{35,36} approximations both $\underline{\Sigma}$ and $\underline{\Sigma}_{\text{e-ph}}$ in Equation (4) are local.

Every quantity $\underline{\mathbf{X}}$ with an underline denotes the so-called *Keldysh structure*, namely

$$\underline{\mathbf{X}} \equiv \begin{pmatrix} \mathbf{X}^{\text{R}} & \mathbf{X}^{\text{K}} \\ \mathbf{0} & \mathbf{X}^{\text{A}} \end{pmatrix} \quad (5)$$

with $\mathbf{X}^{\text{R,A,K}}$ being the *retarded*, *advanced* and *Keldysh* components where $\mathbf{X}^{\text{K}} \equiv \mathbf{X}^> + \mathbf{X}^<$ and \mathbf{X}^{\geq} being the *greater* and *lesser* components. Each of the Keldysh components in Equation (5) is a matrix in the *Floquet indices*.^{23,25,26,37-39} However, given the time-translation invariant character of the problem at hand,^{25,26,38} only the diagonal components and especially the *time-averaged* element $\underline{\mathbf{X}}_{00}$ will be non-vanishing. For this reason we will omit the subscript in the rest of the Manuscript.

Details concerning the computation of the electron-phonon SE $\underline{\Sigma}_{\text{e-ph}}$ within the Migdal approximation can be found in our previous work.^{23,26}

We recall the definition of the electron spectral function

$$A(\omega) \equiv -\frac{1}{\pi} \text{Im} [G_{\text{loc}}^{\text{R}}(\omega)], \quad (6)$$

where

$$G_{\text{loc}}^{\text{R}}(\omega) = \int d\epsilon \int d\bar{\epsilon} \rho(\epsilon, \bar{\epsilon}) \left\{ [G^{-1}(\omega, \epsilon, \bar{\epsilon})]^{\text{R}} \right\}^{-1} \quad (7)$$

$\left\{ [G^{-1}(\omega, \epsilon, \bar{\epsilon})]^{\text{R}} \right\}^{-1}$ being the inverse time-averaged retarded component of the GF in Equation (4). In terms of the *contour-times* z, z' , and in the Migdal approximation, the electron-phonon SE reads

$$\Sigma_{\text{e-ph}}(z, z') = i g^2 G_{\text{loc}}(z, z') D_{\text{ph}}(z, z') \quad (8)$$

and corresponds to the lowest-order diagram in the phonon propagator D_{ph} , the form of which will be discussed below. $G_{\text{loc}}(z, z')$ is the contour-times local GF, the retarded component of which obeys Equation (7). The *retarded* and *Keldysh* components of Equation (8) can be found in our previous work.²⁶ In this Manuscript we will use the *wide band limit* approximation⁴⁰ for the heat bath described by \hat{H}_{bath} according to which $\Sigma_{\text{bath}}^{\text{R}}$ reads

$$\Sigma_{\text{bath}}^{\text{R}}(\omega) = -i \frac{\Gamma_{\text{e}}}{2}, \quad (9)$$

where Γ_{e} is the so-called electronic dephasing rate.²³ The Keldysh component of the heat bath SE $\Sigma_{\text{bath}}^{\text{K}}(\omega)$ is obtained by the fluctuation dissipation theorem, i.e. $\Sigma_{\text{bath}}^{\text{K}}(\omega) = 2i \text{Im} [\Sigma_{\text{bath}}^{\text{R}}(\omega)] \tanh[\beta(\omega - \mu)/2]$. Other important observables are the current J flowing in the direction of the applied field and the kinetic energy E_{kin} of the electrons of the lattice: the derivation of both these quantities can be found in Reference.²³

3.1.2 Phonon Dyson equation

The optical phonon branch consists of Einstein phonons coupled to an ohmic bath, the Dyson equation of which reads

$$\underline{D}_{\text{ph}}(\omega) = [\underline{D}_{\text{ph,E}}^{-1}(\omega) - \underline{\Pi}_{\text{bath}}(\omega) - \underline{\Pi}_{\text{e-ph}}(\omega)]^{-1} \quad (10)$$

with the non-interacting retarded component of the Einstein phonon propagator given by

$$D_{\text{ph,E}}^{\text{R}}(\omega) = 2\omega_{\text{E}} / (\omega^2 - \omega_{\text{E}}^2). \quad (11)$$

The Einstein phonon is coupled to an ohmic bath $\hat{H}_{\text{ph,ohm}}$, the real *retarded* GF of which is obtained from the Kramers-Krönig relations,³⁶ while the *Keldysh* component is given by

$$\Pi_{\text{bath}}^{\text{K}}(\omega) = -2\pi i A_{\text{bath}}(\omega) \coth(\beta\omega/2). \quad (12)$$

We choose the following form for the ohmic bath DOS in (12)

$$A_{\text{bath}}(\omega) = \frac{v_{\text{c}}^2}{\omega_{\text{c}}} \left[\frac{1}{1 + \left(\frac{\omega - \omega_{\text{c}}}{\omega_{\text{c}}}\right)^2} - \frac{1}{1 + \left(\frac{\omega + \omega_{\text{c}}}{\omega_{\text{c}}}\right)^2} \right], \quad (13)$$

where $-\pi A_{\text{bath}}(\omega) \equiv \text{Im}[\Pi_{\text{bath}}^{\text{R}}(\omega)]$. In Eq. (13) ω_{c} denotes the ohmic bath cutoff frequency and v_{c} the hybridization strength to the ohmic bath.

According to the DMFT approximation, the polarization diagram $\Pi_{\text{e-ph}}$ only depends on the local electron GF. Within the Migdal approximation, the contour times *polarization* diagram^{35,36} in Equation (10) reads

$$\Pi_{\text{e-ph}}(z, z') = -2i g^2 G_{\text{loc}}(z, z') G_{\text{loc}}(z', z) \quad (14)$$

with the factor 2 accounting for spin degeneracy. We denote the scheme in which $\Pi_{\text{e-ph}}(z, z')$ is set to zero as non-self-consistent (NSC) while within the self-consistent (SC) treatment the phonon SE in Equation (14) is non-vanishing. The real time components of Equation (14) have been derived in previous work from the authors.²³

3.2 IPT impurity solver and DMFT loop

The IPT impurity solver is based on the perturbative expansion of the electron SE in terms of the so called *Weiss field* $\underline{\mathcal{G}}_0^{-1}(t, t') \equiv g_0^{-1}(t, t') - \underline{\Delta}(t, t')$,¹⁷ namely

$$\Sigma^{\lessgtr}(t, t') = U^2 \mathcal{G}_0^{\lessgtr}(t, t') \mathcal{G}_0^{\gtrless}(t', t) \mathcal{G}_0^{\lessgtr}(t, t'), \quad (15)$$

with the *retarded* and *Keldysh* components obtained as

$$\begin{aligned} \Sigma^{\text{R}}(t, t') &= \theta(t - t') (\Sigma^>(t, t') - \Sigma^<(t, t')) \\ \Sigma^{\text{K}}(t, t') &= \Sigma^>(t, t') + \Sigma^<(t, t'). \end{aligned} \quad (16)$$

At the steady-state all the quantities in Equation (16) are dependent on the difference $t - t'$ alone so that they can be easily Fourier-transformed to the frequency domain. The *retarded* and *Keldysh* components of the Weiss field then read

$$\begin{aligned} \mathcal{G}_0^{\text{R}}(\omega) &= \frac{1}{\Sigma^{\text{R}}(\omega) + G_{\text{loc}}^{-1, \text{R}}(\omega)}, \\ \mathcal{G}_0^{\text{K}}(\omega) &= -|\mathcal{G}_0^{\text{R}}(\omega)|^2 \left(\Sigma^{\text{K}}(\omega) - \frac{G_{\text{loc}}^{\text{K}}(\omega)}{|G_{\text{loc}}^{\text{R}}(\omega)|^2} \right). \end{aligned} \quad (17)$$

At half-filling the Hartree term $U/2$ must be explicitly added to $\Sigma^{\text{R}}(\omega)$ before computing the quantities in Equation (17). The main steps of DMFT employing the IPT are:

- i. Guess $\underline{\Sigma}(\omega)$, $\underline{\Sigma}_{\text{e-ph}}(\omega)$ and $\underline{\Pi}_{\text{e-ph}}(\omega)$
- ii. Compute $\underline{G}_{\text{loc}}(\omega)$ and $\underline{D}_{\text{ph}}(\omega)$ as in Equation (7) and (10)
- iii. Extract $\mathcal{G}_0^{\lessgtr}(\omega) = [\mathcal{G}_0^{\text{K}}(\omega) \mp (\mathcal{G}_0^{\text{R}}(\omega) - \mathcal{G}_0^{\text{A}}(\omega))]/2$ from Eq. (17)
- iv. Fourier-transform $\mathcal{G}_0^{\lessgtr}(\omega)$ to get $\Sigma^{\lessgtr}(t, t')$ as in (15)
- v. Fourier-transform $\underline{G}_{\text{loc}}(\omega)$ and $\underline{D}_{\text{ph}}(\omega)$, compute $\Sigma_{\text{e-ph}}^{\text{R/K}}(t, t')$ and $\Pi_{\text{e-ph}}^{\text{R/K}}(t, t')$
- vi. Update $\underline{\Sigma}(\omega)$, $\underline{\Sigma}_{\text{e-ph}}(\omega)$ and $\underline{\Pi}_{\text{e-ph}}(\omega)$ via back Fourier-transform.

The steps ii. to vi. are then repeated until convergence.

4 Results

In this section we discuss the results of the IPT impurity solver for the system at hand.

U/t^*	ε_c/t^*	μ/t^*	β/t^{*-1}	ω_c/t^*	v_c/t^*	g/t^*	ω_{E}/t^*
8	-4	0	20	0.6	0.055	0.4	0.6

Table 1: Default parameters for the main variables used in this Manuscript.

4.1 Einstein phonons

The current J and kinetic energy E_{kin} as functions of the applied field F for both the SC and NSC schemes are shown in **Figure 1**. We observe that the SC scheme has no effect for field strengths $F < U/2$, for which the SC and NSC curves for both J and E_{kin} lie on top of each other. On the other hand, the SC scheme does contribute corrections, albeit tiny, once the field F runs past the resonance $U/2$. In particular the peak values at $F \approx U$ are lowered with respect to the NSC treatment, whereas the values around them are a bit smeared out. The overall behavior observed here is qualitatively in agreement

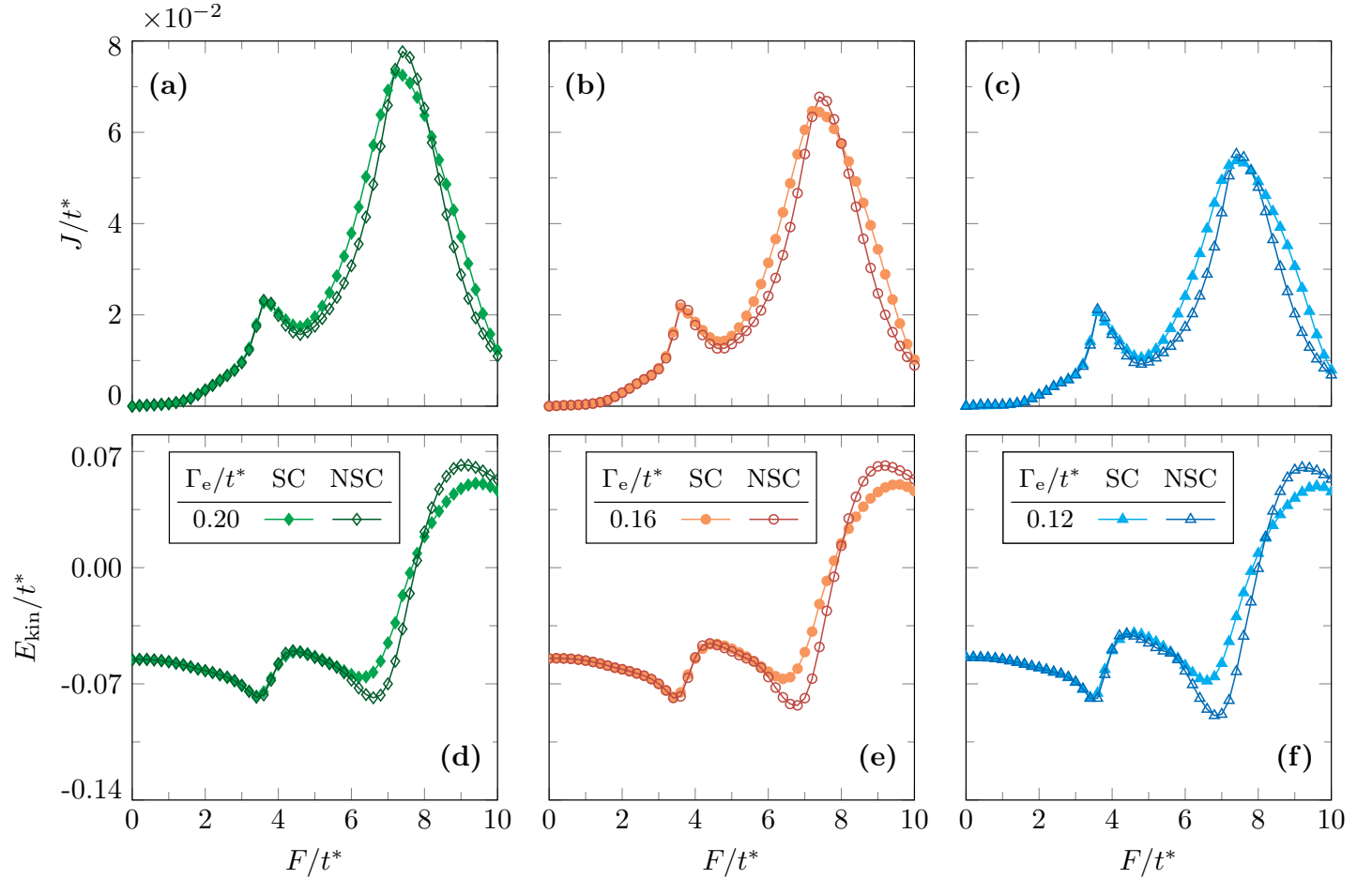


Figure 1: Current J as function of the applied field F for (a) $\Gamma_e = 0.20t^*$ (b) $\Gamma_e = 0.16t^*$ and (c) $\Gamma_e = 0.12t^*$ for both SC and NSC phonons. Panels (d), (e) and (f) show the kinetic energy E_{kin} for the same coupling strengths, respectively. Default parameters are specified in Table 1.

with the results presented in Reference.²³ Also, the order of magnitude of both J and E_{kin} quantitatively agrees with the solution obtained within the AMEA solver. However, within the IPT the two main resonances $F \approx U/2$ and $F \approx U$ are shifted towards smaller field strengths and the differences between the SC and NSC schemes are not as distinguished as they are when using AMEA.

In **Figure 2** is displayed the behavior of J and E_{kin} as function of the applied field for selected values of U , see panels (a) and (b) for the NSC scheme and (c) and (d) for SC treatment. We observe that in the SC case the current and kinetic energy curves are broadened, see panels (b) and (d). Once again, we stress the qualitative agreement between the results presented in **Figure 2** and those presented in Reference.²³ In particular we observe the increase in the current corresponding to the peak at $F \approx U/2$ as the Hubbard U is decreased for both NSC and SC schemes. Also, while the two peaks at $U/2$ and U stays approximately the same in height, we find that the SC treatment enhances J for field strengths that lie in between the two main resonances. Finally, also the kinetic energy preserves the overall behavior described in previous work.²³

Figure 3 shows electron spectral function at $F = 0$ within the (a) NSC and (b) SC schemes for both the IPT and AMEA impurity solvers. The IPT-resolved spectral function shows a much more prominent *quasi-particle* peak at around $\omega = 0$ ²⁶ as the Hubbard U is reduced, and an underestimation of the width of the Hubbard bands within both the NSC and SC treatment. On the other hand, at $U = 8t^*$ the height of the *quasi-particle* peaks obtained in IPT and AMEA are in quite good agreement, even though the Hubbard bands are still narrower within the IPT than in the AMEA case.

4.2 The threshold field

In models of band insulators (those in which the opening of a band gap is not due to correlation effects among electrons), one expects the J - F curve to display the *threshold* behavior³²

$$J \propto F \exp(-F_{\text{th}}/F), \quad (18)$$

due to the opening of a gap that prevents electrons from making the transition from the valence to the conduction band. Equation (18) shows that only when the applied field runs past the threshold field F_{th} electrons can cross the band gap, giving rise to a steady-state current. By determining the threshold field F_{th} one can infer the magnitude of the *effective* band gap of the model. In previous work by the authors,²³ it has been shown that in strongly correlated systems the threshold behavior in Equation (18) does not hold for small field strengths, due to the presence of resonances at $F \approx U/n$ with $n \in \mathbb{N}$.^{6,26} By using the IPT impurity solver instead, one loses part of the information about the electronic correlation due to the fact that the electron SE is constructed from a noninteracting GF, the Weiss field in Equation (15).

In order to highlight the differences between a semiconductor model (band insulator) and strongly correlated systems, we benchmark the results for $U/t^* = \{5, 6, 7, 8\}$ obtained within the IPT impurity solver against a linear regression fit according to Equation (18), limited to small inverse field strengths. **Figure 4(a)** shows the ratio J/F as function of the inverse field $1/F$ within SC and NSC schemes: the values of the inverse field used in the fit can be deduced by the extent of the black line. The threshold fields obtained with the linear regression fit are shown in Figure 4(b): the back-action from electrons onto phonons does not affect the results within the numerical accuracy, thus leaving the threshold fields unaltered. As expected, a larger F_{th} is required to compensate a larger band gap and promote particles across it. However, due to the extension of the Hubbard bands the *effective* gap is reduced and the threshold field is much lower than the nominal value of the Hubbard U .

5 Conclusion

In this Manuscript a Mott insulating system has been characterized in terms of its conducting properties when subject to an external static electric. Optical phonons and electronic heat bath provide the relaxation pathways for the extra energy injected by the field, so that the electron of the lattice can relax back to the valence band and a steady-state current be established.

The iterated perturbation theory (IPT) approach has been used as impurity solver to address the steady-state of the system. The corresponding results have been benchmarked against those obtained within a much more computationally costly one developed by the authors, the so-called auxiliary master equation approach (AMEA) impurity solver. It has been shown that the results obtained by the IPT solver qualitatively agree with those given by the AMEA solver even though the former approach does not capture the resonances in the current characteristics which are directly related to the correlated nature of the electrons of the lattice. Being computationally cheaper, the IPT solver could be used to span the parameter space when investigating novel setups and gather information about the interesting regions to be addressed by a more reliable and computationally costly impurity solver.

Acknowledgements

This research was funded by the Austrian Science Fund (Grant No. P 33165-N) and by NaWi Graz. The results have been obtained using the Vienna Scientific Cluster and the D-Cluster Graz.

References

- [1] C. Aron, *Phys. Rev. B* **2012**, *86* 085127.
- [2] A. Amaricci, C. Weber, M. Capone, G. Kotliar, *Phys. Rev. B* **2012**, *86* 085110.
- [3] C. Aron, G. Kotliar, C. Weber, *Phys. Rev. Lett.* **2012**, *108* 086401.

- [4] J. Li, C. Aron, G. Kotliar, J. E. Han, *Phys. Rev. Lett.* **2015**, *114* 226403.
- [5] J. E. Han, J. Li, C. Aron, G. Kotliar, *Phys. Rev. B* **2018**, *98* 035145.
- [6] Y. Murakami, P. Werner, *Phys. Rev. B* **2018**, *98* 075102.
- [7] P. A. Lee, T. V. Ramakrishnan, *Rev. Mod. Phys.* **1985**, *57* 287.
- [8] D. Belitz, T. R. Kirkpatrick, *Rev. Mod. Phys.* **1994**, *66* 261.
- [9] P. Stoliar, L. Cario, E. Janod, B. Corraze, C. Guillot-Deudon, S. Salmon-Bourmand, V. Guiot, J. Tranchant, M. Rozenberg, *Advanced Materials* **2013**, *25*, 23 3222.
- [10] E. Janod, J. Tranchant, B. Corraze, M. Querré, P. Stoliar, M. Rozenberg, T. Cren, D. Roditchev, V. T. Phuoc, M.-P. Besland, L. Cario, *Advanced Functional Materials* **2015**, *25*, 40 6287.
- [11] W. Metzner, D. Vollhardt, *Phys. Rev. Lett.* **1989**, *62* 324.
- [12] A. Georges, G. Kotliar, *Phys. Rev. B* **1992**, *45* 6479.
- [13] A. Georges, G. Kotliar, W. Krauth, M. J. Rozenberg, *Rev. Mod. Phys.* **1996**, *68* 13.
- [14] G. Kotliar, S. Y. Savrasov, K. Haule, V. S. Oudovenko, O. Parcollet, C. A. Marianetti, *Rev. Mod. Phys.* **2006**, *78*, 3 865.
- [15] J. K. Freericks, V. M. Turkowski, V. Zlatić, *Phys. Rev. Lett.* **2006**, *97*, 26 266408.
- [16] H. Aoki, N. Tsuji, M. Eckstein, M. Kollar, T. Oka, P. Werner, *Rev. Mod. Phys.* **2014**, *86* 779.
- [17] H. Kajueter, G. Kotliar, *Phys. Rev. Lett.* **1996**, *77* 131.
- [18] E. Arrigoni, M. Knap, W. von der Linden, *Phys. Rev. Lett.* **2013**, *110* 086403.
- [19] A. Dorda, M. Nuss, W. von der Linden, E. Arrigoni, *Phys. Rev. B* **2014**, *89* 165105.
- [20] A. Dorda, M. Ganahl, H. G. Evertz, W. von der Linden, E. Arrigoni, *Phys. Rev. B* **2015**, *92* 125145.
- [21] I. Titvinidze, A. Dorda, W. von der Linden, E. Arrigoni, *Phys. Rev. B* **2015**, *92* 245125.
- [22] D. Werner, J. Lotze, E. Arrigoni, *Phys. Rev. B* **2023**, *107* 075119.
- [23] T. M. Mazzocchi, D. Werner, P. Gazzaneo, E. Arrigoni, *Phys. Rev. B* **2023**, *107* 155103.
- [24] V. M. Turkowski, J. K. Freericks, *Phys. Rev. B* **2006**, *73*, 7 075108.
- [25] N. Tsuji, T. Oka, H. Aoki, *Phys. Rev. B* **2008**, *78*, 23 235124.
- [26] T. M. Mazzocchi, P. Gazzaneo, J. Lotze, E. Arrigoni, *Phys. Rev. B* **2022**, *106* 125123.
- [27] J. Schwinger, *J. Math. Phys.* **1961**, *2* 407.
- [28] L. V. Keldysh, *Sov. Phys. JETP* **1965**, *20* 1018.
- [29] J. Rammer, H. Smith, *Rev. Mod. Phys.* **1986**, *58* 323.
- [30] H. Haug, A.-P. Jauho, *Quantum Kinetics in Transport and Optics of Semiconductors*, Springer, Heidelberg, **1998**.
- [31] G. Stefanucci, R. van Leeuwen, *Nonequilibrium Many-Body Theory of Quantum Systems: A modern introduction*, Cambridge University Press, Cambridge, **2013**.
- [32] M. Eckstein, P. Werner, *J. Phys.: Conf. Series* **2013**, *427* 012005.
- [33] M. I. Díaz, J. E. Han, C. Aron, *Phys. Rev. B* **2023**, *107* 195148.

- [34] J. E. Han, C. Aron, X. Chen, I. Mansaray, J.-H. Han, K.-S. Kim, M. Randle, J. P. Bird, *Nature Communications* **2023**, *14*, 1.
- [35] Y. Murakami, P. Werner, N. Tsuji, H. Aoki, *Phys. Rev. B* **2015**, *91* 045128.
- [36] Y. Murakami, N. Tsuji, M. Eckstein, P. Werner, *Phys. Rev. B* **2017**, *96* 045125.
- [37] A. V. Joura, J. K. Freericks, T. Pruschke, *Phys. Rev. Lett.* **2008**, *101*, 19 196401.
- [38] M. E. Sorantin, A. Dorda, K. Held, E. Arrigoni, *Phys. Rev. B* **2018**, *97* 115113.
- [39] P. Gazzaneo, T. M. Mazzocchi, J. Lotze, E. Arrigoni, *Phys. Rev. B* **2022**, *106* 195140.
- [40] J. Neumayer, E. Arrigoni, M. Aichhorn, W. von der Linden, *Phys. Rev. B* **2015**, *92* 125149.

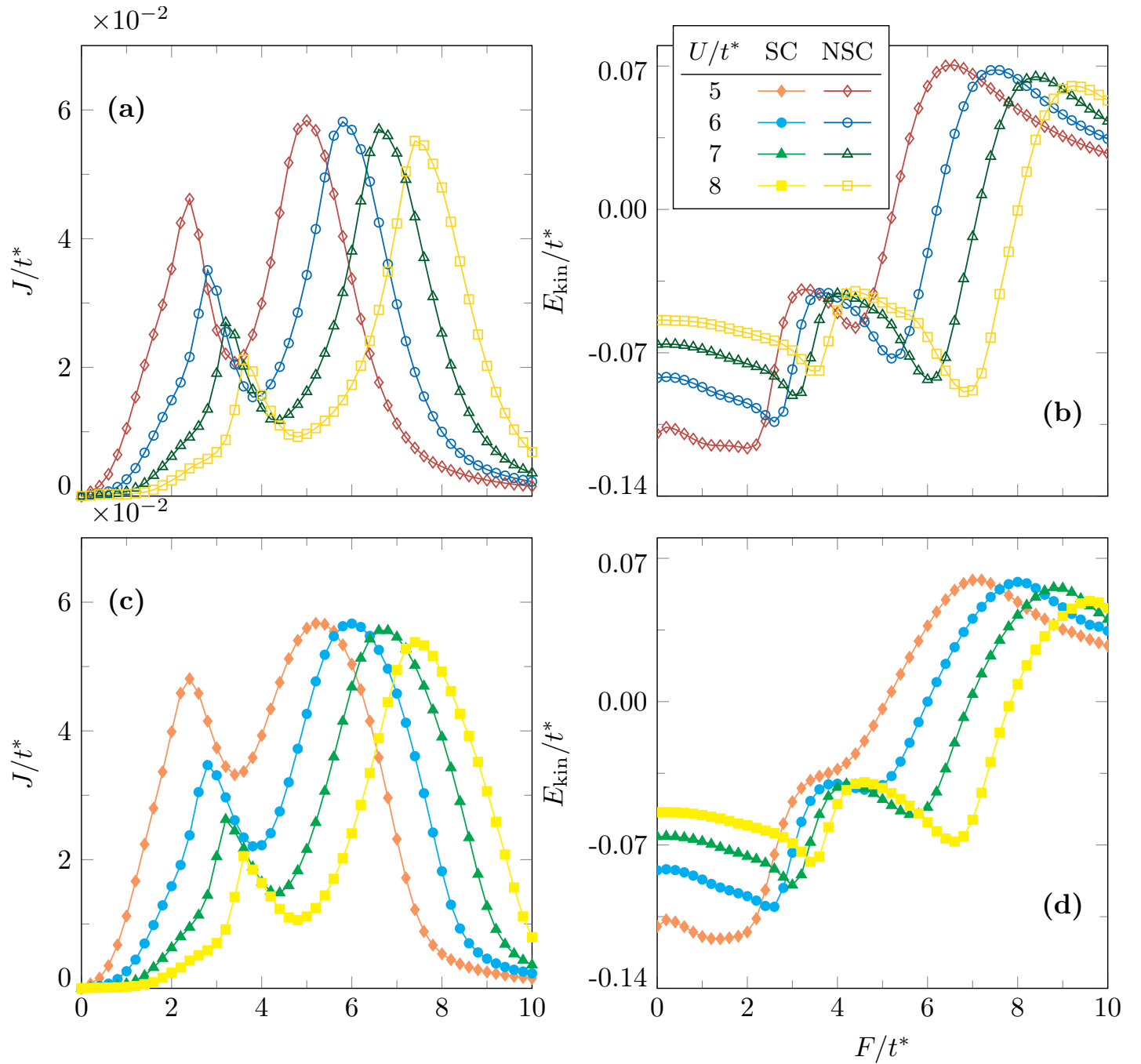


Figure 2: Current J within (a) NSC and (c) SC scheme for selected values of the Hubbard U as function of the applied field F . Kinetic energy E_{kin} against the applied field F is shown for (b) the NSC and (d) the SC scheme for the same values of the Hubbard U . Default parameters are specified in Table 1. (Here $\Gamma_e = 0.12t^*$.)

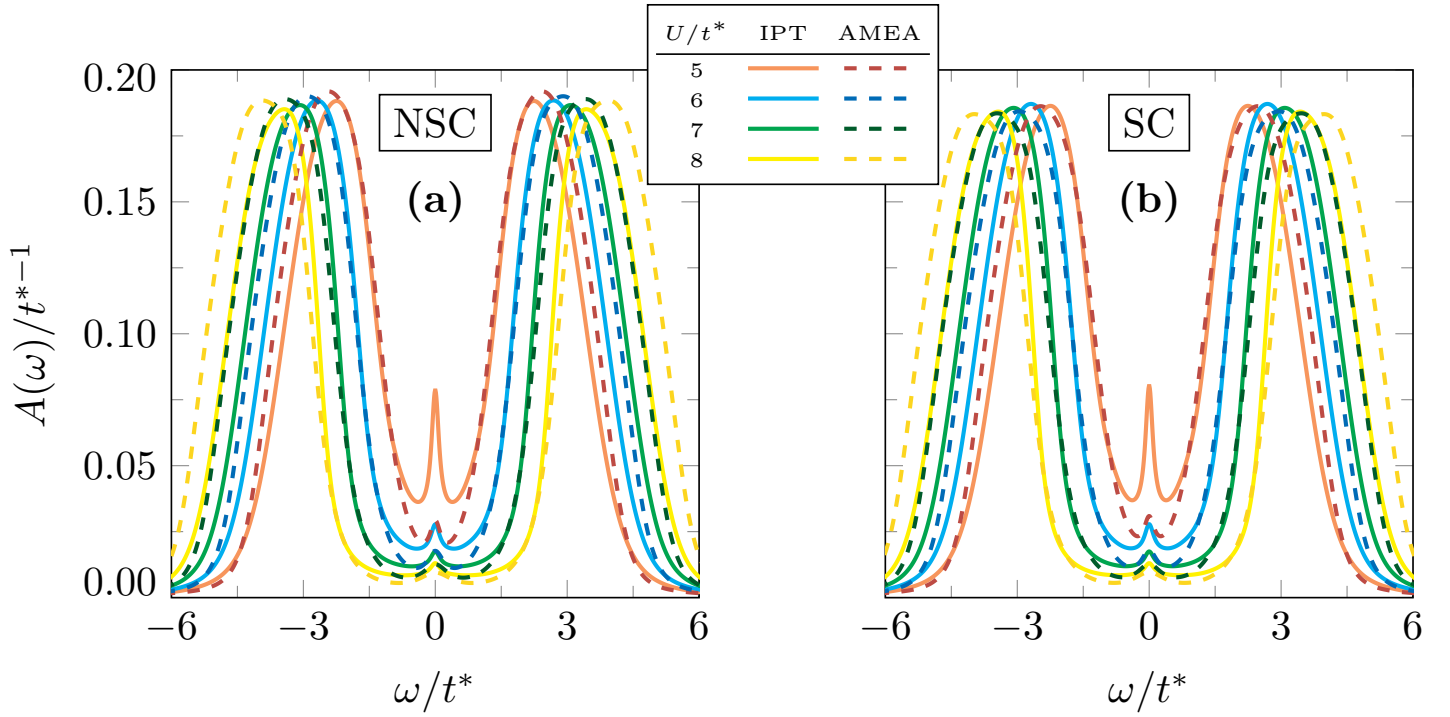


Figure 3: Electron spectral function $A(\omega)$ at $F = 0$ for the (a) NSC and (b) SC scheme as function of selected values of the Hubbard U obtained within the IPT and AMEA. Default parameters are specified in Table 1. (Here $\Gamma_e = 0.12t^*$.)

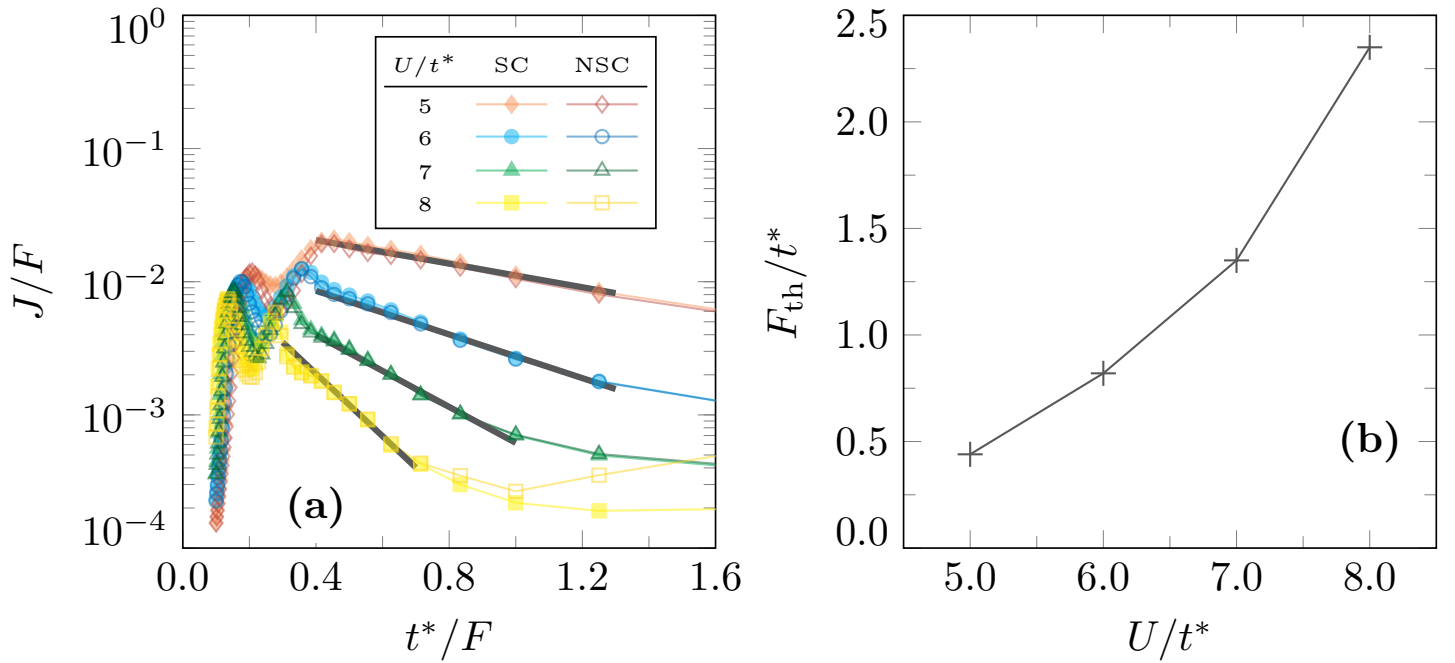
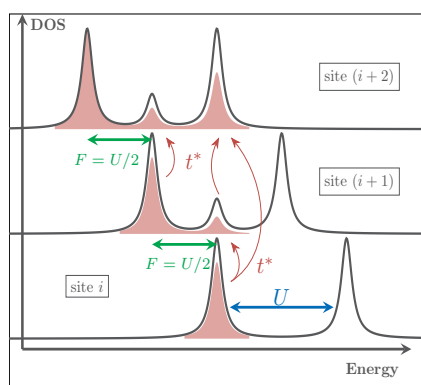


Figure 4: (a) Ratio J/F as function of the inverse field $1/F$ for selected values of the Hubbard U within the NSC and SC schemes obtained with IPT impurity solver. Black straight lines extend over the range of values of $1/F$ used for the linear regression fit yielding the threshold field F_{th} as function of U shown in panel (b). The SC treatment has no effect on F_{th} , which is the reason why panel (b) does not distinguish between the two cases. Default parameters are specified in Table 1. (Here $\Gamma_e = 0.12t^*$.)

Table of Contents



Schematic representation of the current flowing within the lattice. When the field is applied electrons can tunnel through the former gap of an adjacent site, creating the necessary states to populate the conduction band of a site which is twice lattice spacings apart.